

## Future Dynamics of the Local Group. I. MW-M31 Interactions

COLIN LEACH 

### ABSTRACT

**TODO** Add a concise and intelligent summary of the paper, once I get a clearer idea what it will include (and how to seem intelligent).

**Keywords:** Galaxy Merger – Local Group – Stellar Disk – Stellar Bulge – Dark Matter Halo – Hernquist Profile – Merger Remnant

### 1. INTRODUCTION

The currently-accepted model of galaxy formation involves baryonic matter (gas and dust) falling into gravitational potential wells created by local over-densities in the Dark Matter (DM). Further gravitational collapse and Jeans fragmentation can then lead to creation of galaxies and stars (Mo et al. 2010).

However, decades of observational and theoretical studies tell us that, firstly, this by itself does not account for the wide range of galaxy morphologies seen at all epochs; secondly, there is no reason to suppose that galaxies continue in serene isolation after their formation.

Attempts to model interactions and mergers between galaxies with numerical simulations goes back at least to Toomre & Toomre (1972). This field continues to develop, with improvements in both hardware and algorithms allowing larger particle numbers in N-body simulations and more sophisticated treatment of gas hydrodynamics, magnetic fields and other factors (Bodenheimer et al. 2007).

As with all theoretical studies, it is vital to stay connected to the best experimental data as this constantly evolves, constantly comparing models against observations. Checking simulations against high-redshift galaxies is necessary but inevitably approximate. A perhaps more rigorous test is to model the galaxies for which we have the most precise and detailed observational measurements: those which are (by far) closest to us.

The largest galaxies in our Local Group (LG) are the Milky Way (MW), Andromeda (M31) and Triangulum (M33). A simulation of MW–M31–M33 orbital evolution was described previously in Marel et al. (2012a), hereafter vdM12. That paper included an extensive analysis of both N-body simulations and semi-analytic orbit integrations. The present study uses data from the

same N-body simulation to carry out further computational analysis.

The simulation was based on data in Marel et al. (2012b) suggesting that M31 is approaching the MW directly with little proper motion detected by Hubble Space Telescope studies. Recent data from Gaia DR2 (Brown et al. 2018) suggest that infall is slightly less radial than previously thought (Marel et al. 2019), leading to a slightly later first approach with a larger pericenter distance. However, detailed simulations based on that new data have not yet been carried out.

This paper will review the initial conditions and time evolution for multiple physical parameters of the simulation. Particular attention will be paid to the first MW–M31 close approach around 4 Gyr, the second approach and merger around 6 Gyr, and the structure and dynamics of the post-merger remnant.

Time probably precludes much analysis of the fate of M33, which will need to be the subject of a future paper.

#### 1.1. Data

Data from one N-body simulation in vdM12 was supplied in text-file format by one of the original authors. This included position and velocity data for each particle at the current epoch ( $t = 0$ ) and 800 future time steps. For ease of analysis, this was all transferred to the open source database PostgreSQL<sup>1</sup> (approximately 1.35 billion records). The same database was used to store computed summary data during the analysis.

Particle counts for each time point are shown in Table 1 and total masses in Table 2. We can see that total mass is the same for MW/M31 but our galaxy has more dark matter (lower baryon fraction) and M31 has more

<sup>1</sup> <http://www.postgresql.org>

**Table 1.** Particle counts

| Galaxy | DM Halo | Disk      | Bulge   | Total     |
|--------|---------|-----------|---------|-----------|
| MW     | 250,000 | 375,000   | 50,000  | 675,000   |
| M31    | 250,000 | 600,000   | 95,000  | 945,000   |
| M33    | 25,000  | 46,500    | 0       | 71,500    |
| LG     | 525,000 | 1,021,500 | 145,000 | 1,691,500 |

luminous stars (higher baryon fraction). M33 is about 10-fold lighter than either.

**Table 2.** Aggregate masses ( $M_{\odot} \times 10^{12}$ )

| Galaxy | DM Halo | Disk  | Bulge | Total |
|--------|---------|-------|-------|-------|
| MW     | 1.975   | 0.075 | 0.010 | 2.060 |
| M31    | 1.921   | 0.120 | 0.019 | 2.060 |
| M33    | 0.187   | 0.009 | 0.000 | 0.196 |
| LG     | 4.082   | 0.204 | 0.029 | 4.316 |

The coordinate system is approximately centered on the Milky Way at  $t = 0$ . The center of mass (CoM) of all particles in the system is not fixed over time, moving at an average of  $\vec{v} = \langle 35.9, -26.7, 27.5 \rangle$  km/s with some minor fluctuations due to numerical approximations. In contrast, the total angular momentum of the system is very small at all time points.

### 1.2. Software

The work in this report was carried out in Python using standard packages. Full details are available online<sup>2</sup>

## 2. RESULTS

### 2.1. Trajectories

The simulation does not explicitly include a supermassive black hole (SMBH) at the center of each galaxy, but the galactic center was defined by calculating the center of mass (CoM) of the disk particles and iteratively constraining the radius of interest until convergence.

To plot motions of the three galactic CoMs it is convenient to transform to a coordinate system in which at  $t = 0$  they all lie in the  $x, y$  plane with MW and M31 on the  $x$ -axis. The overall CoM is moving, as noted above,

so at each time point the coordinates are translated to center it at the origin.

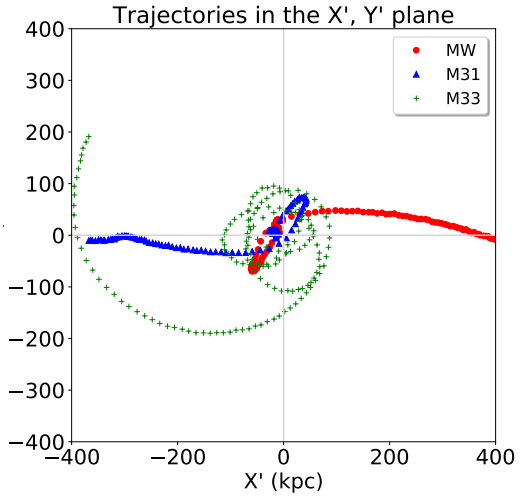


**Figure 1.** Trajectories of each galactic center of mass in the  $X', Y'$  plane. Points are at 71 Myr intervals.

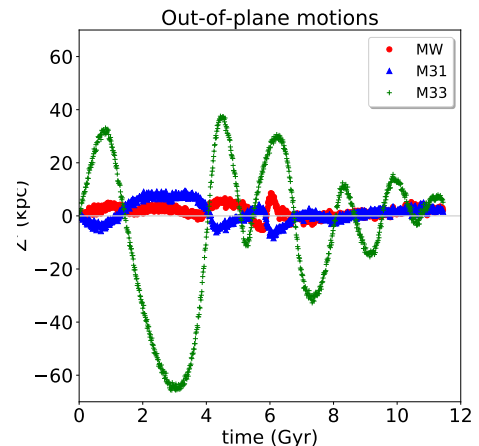


**Figure 2.** Trajectories of each galactic center of mass perpendicular to the  $X', Y'$  plane.

In vdM12 this is referred to as the  $X', Y', Z'$  coordinate system and their figure 2 shows multiple views of how the galaxies move through time. In this paper, Figures 1 and 2 show some alternative views in essentially the same coordinates (up to a sign; the  $x$  and  $z$  axes are flipped). Figure 1 reproduces the top left panel of vdM12. Figure 2 shows that MW and M31 remain close to the starting plane while M33 has larger, irregular out-of-plane motions.

<sup>2</sup> Code [https://github.com/colinleach/400B\\_Leach](https://github.com/colinleach/400B_Leach)  
documentation <https://400b-leach.readthedocs.io>

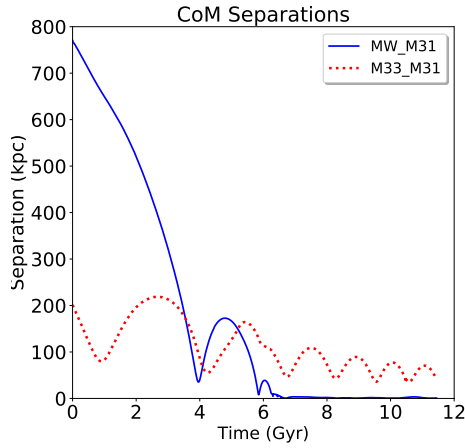


**Figure 3.** Separations of galactic CoMs.

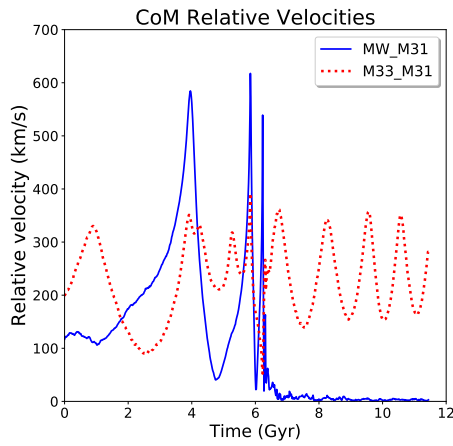


**Figure 4.** Relative velocities of galactic CoMs.

Relative motions of the CoMs are shown against time in Figures 3 and 4, equivalent to figures 3 and 4 in vdM12.

There is a MW-M31 close approach with first pericenter at 3.96 Gyr with a minimum separation of 35.1 kpc, then a separation to 173 kpc at apocenter and finally a convergence to 7.8 kpc at second pericenter and merger between 5.9 - 6.5 Gyr. Relative velocities spike sharply during these approaches, as potential energy is converted to kinetic energy, before declining to essentially zero.

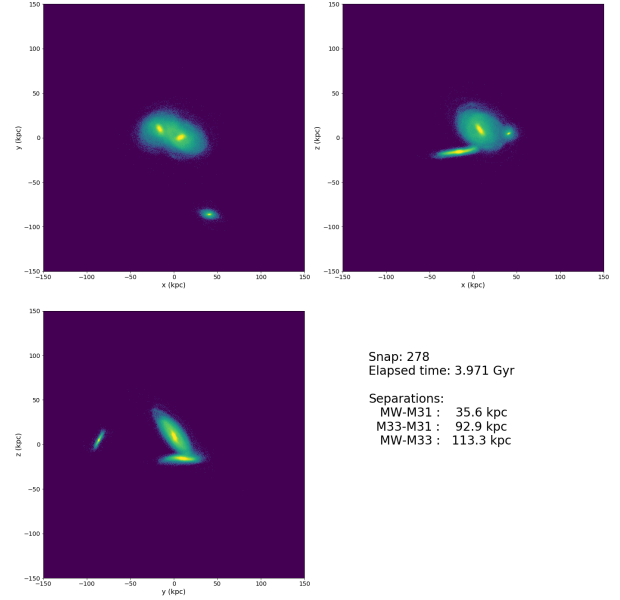


**Figure 5.** Orthogonal views of the three galaxies (disk particles only) at first apocenter. **TODO** improve this visually!

Figure 5 shows a view of first apocenter as a disk density plot from three orthogonal directions. The full animation is available online<sup>3</sup>

Meanwhile, in this simulation run M33 remains separate throughout, albeit on a decaying orbit. In vdM12 the authors investigate the effect of small changes in initial conditions and estimate a 9% chance of an M33-MW collision at first pericenter, before the M31-MW merger.

## 2.2. Mass profiles and rotation curves

Figure 6 shows the cumulative mass profile, by particle type and in total, for each galaxy. The center of each galaxy is dominated by baryonic matter with the DM halo becoming dominant at larger radii.

<sup>3</sup> [https://github.com/colinleach/400B\\_Leach/blob/master/animations/collisions\\_disk.mp4](https://github.com/colinleach/400B_Leach/blob/master/animations/collisions_disk.mp4)

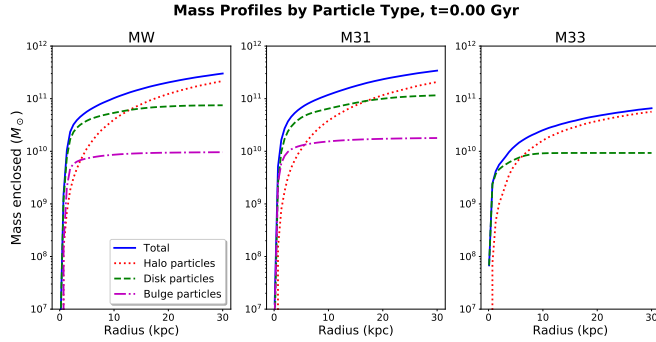


**Figure 6.** Mass profiles for each galaxy at the current epoch.

Figure 7 shows the rotation curves expected from these mass profiles. Without the DM halo the circular velocity would peak within a few kpc of the CoM then fall steadily at larger radii. With the more diffuse DM halo added, we see the relatively flat overall rotation curves which attracted the attention of 20th century astronomers including Zwicky (1933) and Rubin & Ford (1970)

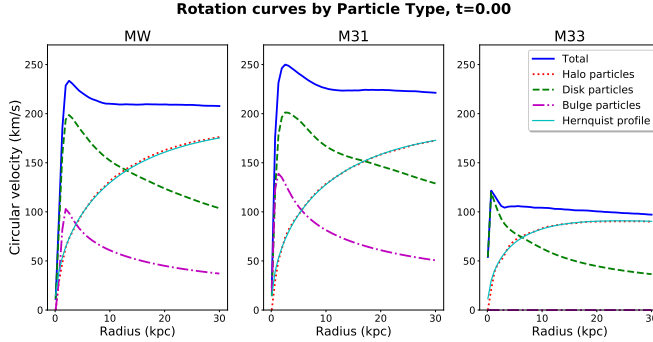


**Figure 7.** Rotation curves for each galaxy at the current epoch.

### 2.3. Stellar disk

#### 2.3.1. Structure

TODO identify the bar?

TODO more on spiral arms

Disk structure and evolution may be easier to visualize if we transform to cylindrical coordinates (with the angular momentum vector along the  $z$ -axis) and use  $r - \theta$  plots. Figure 8 shows this for the two large galaxies at several timepoints (as labelled). Spiral arms show up in both early in the simulation. First pericenter has little effect, but 0.3 Gyr later we see highly prominent tidal

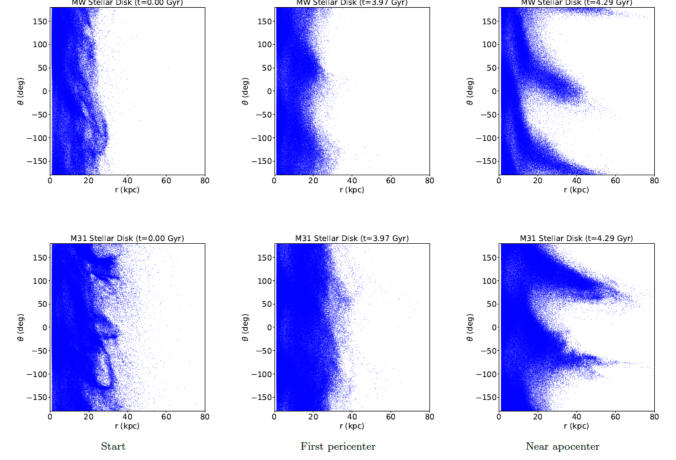


**Figure 8.** Disk particles from MW (top) and M31 (bottom) at three timepoints; cylindrical coordinates.

tails. These images are taken from a full animation for each galaxy, available online<sup>4</sup>

#### 2.3.2. Inclinations

Galactic disks have a well-defined angular momentum vector which is relatively easy to calculate in this type of simulation. Figure 9 shows the angle each makes to the  $X' - Y'$  plane over time.

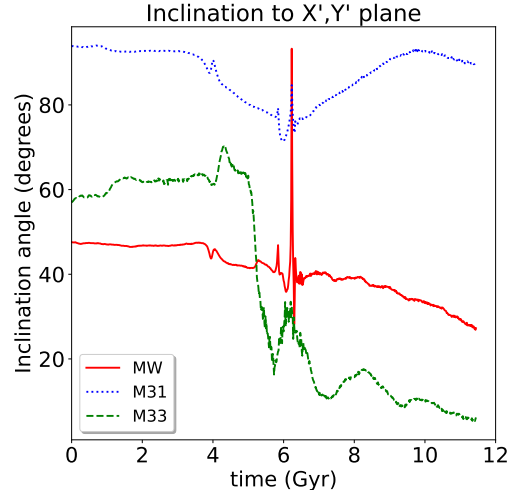


**Figure 9.** Angular momentum inclination angle to the  $X', Y'$  plane for each set of galactic disk particles.

The mutual angle between galactic disks can have a significant impact on how tidal disruption and merger

<sup>4</sup> [https://github.com/colinleach/400B\\_Leach/tree/master/animations/files/cyl\\_M\\*\\_disk.mp4](https://github.com/colinleach/400B_Leach/tree/master/animations/files/cyl_M*_disk.mp4)

dynamics play out **TODO** ref?. This can be calculated from the vector dot products:

$$\theta = \arccos(\hat{L}_1 \cdot \hat{L}_2)$$

Results for the MW-M31 and M33-M31 pairs are shown in Figure 10. For MW-M31, the angle is largely stable until near first pericenter, when tidal forces bring the two disks closer to alignment. This trend continues slowly until near second pericenter. Surprisingly, the angle appears to increase after merger. This suggests either some partitioning of particles of different origin within the remnant, or some addition factor that invalidates this simple analysis. A later section will discuss the complex radial dependency within the remnant, which Figure 10 does not take into account.

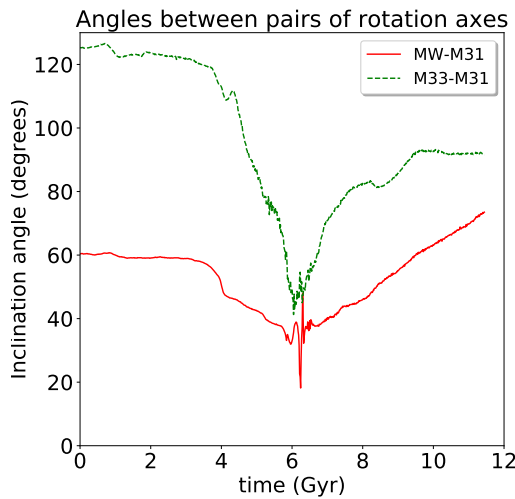


**Figure 10.** Angular momentum angles between pairs of galaxies.

The large variations in M33-M31 angles are indicative of the extensive tidal disruption of the much smaller M33 galaxy. Details are outside the scope of the present paper.

### 2.3.3. Velocity dispersion

The changes in velocity dispersion of disk particles originating from each galaxy are shown in Figure 11. The small periodic oscillation seen from the start, especially in M31, appears to be caused by deviations from radial symmetry in the disk: spiral arms and an increasingly prominent bar. Small MW spikes at initial pericenter (around 4 Gyr) and much larger ones at merger (around 6 Gyr) are clearly visible.

M33 is on an irregular, elliptical and decaying orbit about the MW-M31 merger remnant after about 6.5

Gyr. Velocity dispersion appears to peak at intervals. This perhaps corresponds to successive pericenters when M33 experiences maximal tidal disruption, but this will need further analysis.

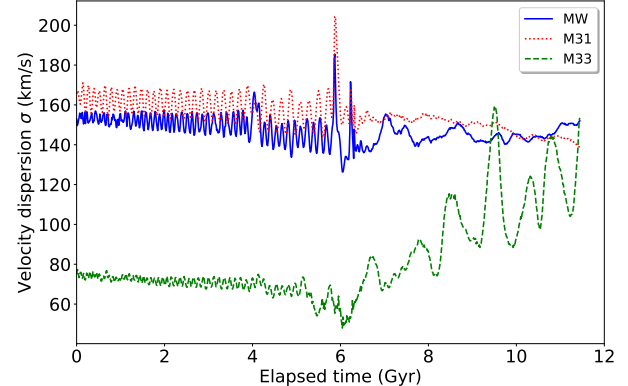


**Figure 11.** Velocity dispersion of disk particles from each galaxy over time.

**TODO** disk rotation curve,  $V_{rot}/\sigma$

### 2.4. Stellar Bulge

A bulge is present in the MW and M31 but not M33. This region of generally older stars extends further above and below the central plane than disk stars. Kinematics of the bulge are more typical of an elliptical galaxy than a spiral disk.

In a study of elliptical galaxies, de Vaucouleurs showed that surface brightness falls off exponentially from the center and approximately as the one-fourth power of radius (de Vaucouleurs 1948). Later work found that this was too restrictive for a wider population of galaxies, so Sérsic generalized the formula to have the inverse exponential  $n$  as an additional free parameter (Sérsic 1963):

$$\log_{10} \left( \frac{I(r)}{I_e} \right) = -3.3307 \left[ \left( \frac{r}{R_e} \right)^{1/n} - 1 \right]$$

Here  $R_e$  is the radius with which half the light is emitted,  $I_e$  is the surface brightness at  $R_e$  and  $n$  is the Sérsic parameter.

This formula is intended for analyzing photographic images and is in terms of light intensity. We have no brightness data in the current simulation, but for systems with few young blue stars we can assume the stellar mass to light ratio  $M_\star/L \sim 1$ . This is probably a reasonable approximation for undisturbed bulges and for an elliptical merger remnant long after the collision.  $R_e$  is then the radius enclosing half the mass.

We can see from Figure 12 that for each galaxy the bulge half-mass radius is fairly stable up to the collision

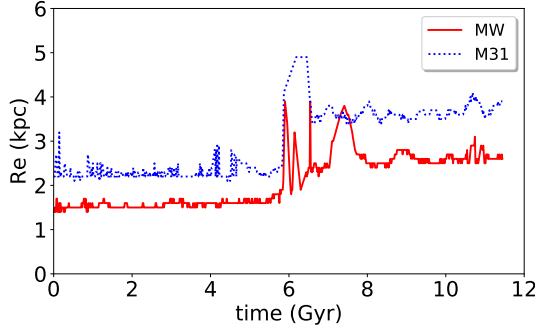


**Figure 12.** Half-mass radius for bulge particles.

and merger of MW and M31. After a period of disturbance, they again become stable at a higher level. The M31 bulge is more diffuse than the MW bulge throughout, and the ex-bulge stars are clearly not randomized in the merger remnant: ex-M31 stars tend towards larger radii than ex-MW stars.

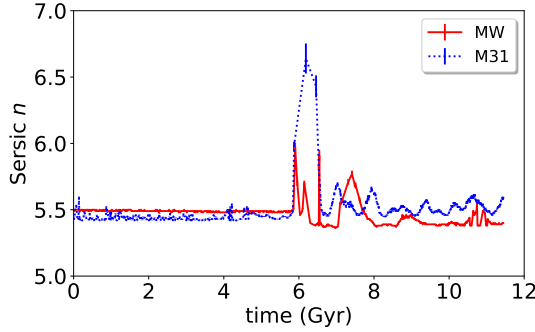


**Figure 13.** Sérsic  $n$  for bulge particles, with  $1\sigma$  error bars.

The Sérsic parameter  $n$  was estimated by a nonlinear least squares fit to the bulge mass profile. As shown in Figure 13 it is fairly constant around 5.5 for any period with meaningful data. The spikes around 6 Gyr should probably be ignored: many values in this collision period are missing, as the least-squares fit failed, and the available data has substantially larger error bars than during stable epochs.

The larger half-mass radius of M31 is reflected in the mass density profile, as shown in Figure 14. MW bulge stars have a higher central peak, M31 bulge stars are more numerous at larger radii. This is true both early in the simulation and in the merger remnant at late times. For both galaxy bulge stars, the central peak is less pronounced post-merger.

The Sérsic fit for both galaxy bulges looks reasonable outside the central density peak, as shown for the MW in Figure 15. The plot for M31 (not included here) is very similar.

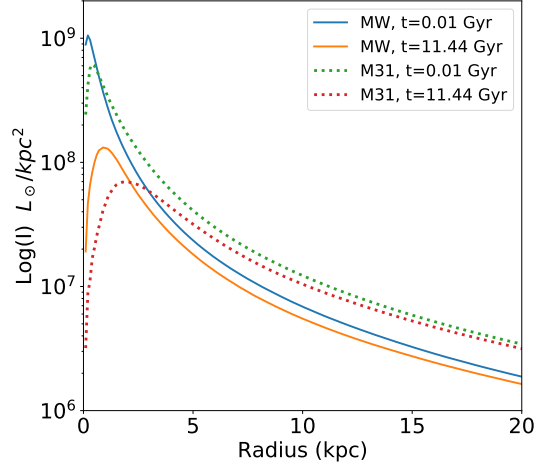


**Figure 14.** Bulge mass density profile for both galaxies at the beginning and end of the simulation.

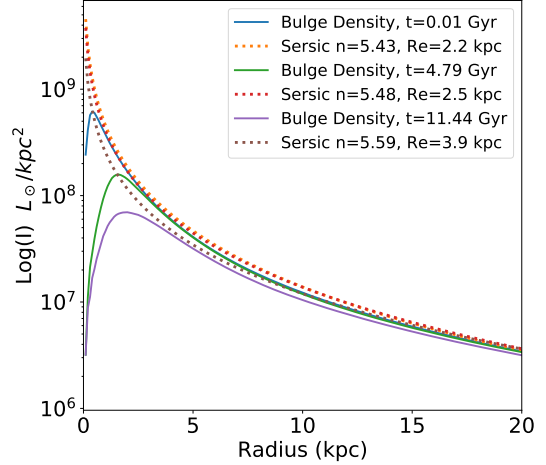


**Figure 15.** MW bulge mass density profiles and Sérsic best fits. Time points are the beginning, the pre-merger pericenter, and the end of the simulation

## 2.5. Dark Matter halo

### 2.5.1. Halo mass profile

Figure 7 also added a theoretical curve in which the DM halo is fitted by a Hernquist profile (Hernquist 1990). The cumulative mass out to radius  $r$  is given by

$$M(r) = M_h \frac{r^2}{(a + r)^2}$$

where  $M_h$  is the total mass of halo particles (see Table 2) and  $a$  is a scale radius which encloses a quarter of the halo mass. Non-linear least squares fitting, similar to that used for Sérsic profiles in a previous section, gave scale radii of 61.1 kpc for MW and M31, 24.3 kpc for M33 at  $t = 0$ .

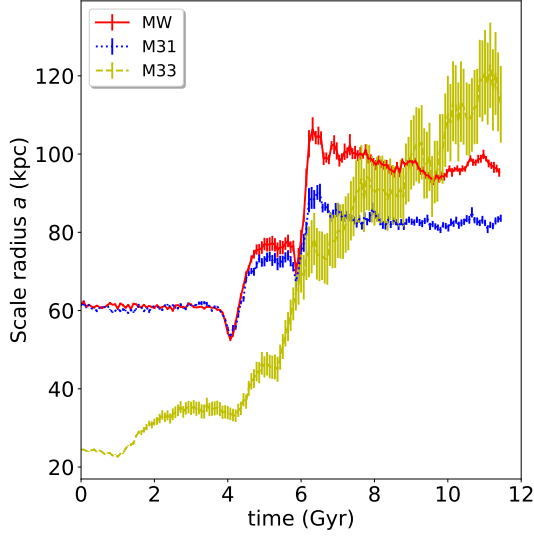


**Figure 16.** Hernquist scale radius  $a$  for DM halo particles originating from each galaxy, with  $1\sigma$  error bars.

Time evolution of the scale radius  $a$  is shown in Figure 16. The MW and M31 remain very similar through first pericenter, then start to diverge with MW particles tending to a larger radius than M31. This becomes most pronounced during and after merger. The dissimilar distribution in the merger remnant will be discussed in a later section.

The scale radius for M33 grows inexorably as the original halo is scattered by tidal forces. Figure 16 also shows the increasingly wide error bars for M33: halo particles for this galaxy are no longer well fitted by a Hernquist profile.

### 2.5.2. Halo rotation

The specific angular momentum  $\vec{h}$  can be calculated from

$$\vec{h} = \frac{\sum_i \vec{r}_i \times m_i \vec{v}_i}{\sum_i m_i}$$

The halo specific angular momentum for each large galaxy is shown in Figure 17. It appears that both are barely rotating at the current epoch, but spin up rapidly during first pericenter and again around the time of merger, as tidal forces convert orbit angular momentum into spin angular momentum. Differences in the remnant will be discussed in a later section

Data for M33 is omitted from Figure 17 for clarity. The spin-up is much more dramatic for this minor galaxy, with peaks approaching  $140 \text{ kpc}^2/\text{Myr}$ , making it unsuitable to plot on the same axes.

**TODO** effect of radius

## 2.6. MW-M31 Close approach

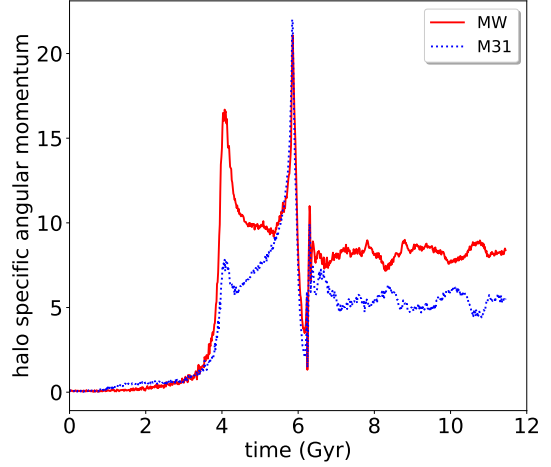


**Figure 17.** Specific angular momentum for halo particles of each galaxy about its CoM ( $\text{kpc}^2/\text{Myr}$ ).

### 2.6.1. Inclinations

The MW and M31 disks have angular momentum vectors inclined at an angle of  $52^\circ$  to each other shortly before pericenter.

**TODO** Clarify prograde/retrograde!

### 2.6.2. Tidal tails and bridges

The presence of long, symmetrical tails giving some galaxies a distinct ‘S’-shape has been described at least as far back as Zwicky (1955). Some astronomers postulated that these were the result of tidal forces during close, glancing encounters, but this was often contested until a detailed computational study by Toomre & Toomre (1972).

Reviewing a broad range of N-body simulations, Barnes & Hernquist (1992) noted that “such features are clearly *relics* of recent collisions rather than ongoing interactions.” In our simulation, both MW and M31 disks remain near-circular during much of the close approach, but conspicuous tails develop as the centers then move further apart: see Figure 8 and the animations referred to in Footnote 3. We also see a more sparsely-populated bridge forming between the galaxies.

To determine the nature and origin of stars in this region, a manual selection was performed as in Figure 18. Stars within the yellow rectangle (left panel) are shown with velocity vectors (center panel) and origin (right panel). Velocities are diverse: mean 195 km/s, range 19–586 km/s.

It appears from the right panel that stars in the tail regions originate in the corresponding disk. The bridge region is more mixed and appears to have a high proportion of former bulge stars. To study this further the coordinate system was transformed to place the large

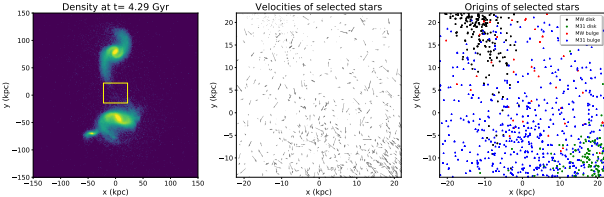


**Figure 18.** Manual selection of bridge particles at 0.33 Gyr after the first MW-M31 pericenter. The left panel shows stellar surface density and the selected region. The center panel shows velocity vectors for these stars and the right panel shows origin by galaxy and particle type. Orientation is with MW top, M31 bottom and M33 lower left.

**TODO** make this page-width in final layout

galaxy CoMs on the  $x$ -axis at  $\pm 64$  kpc, as in Figure 19. It is clear in this view that one MW tail is oriented approximately towards the center of M31.

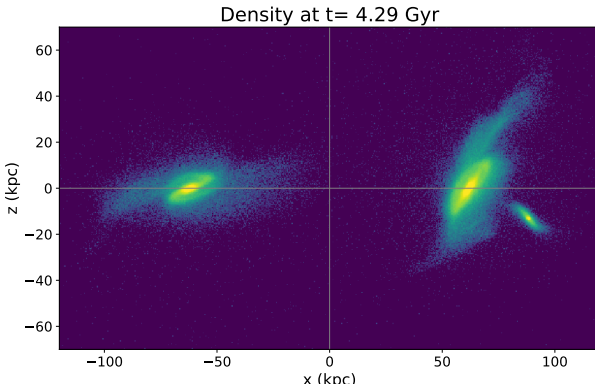


**Figure 19.** View along the midplane between the galactic centers, MW on the left.

**Table 3.** Particle counts close to the midplane

|       | Bulge | Disk | Total |
|-------|-------|------|-------|
| MW    | 305   | 1317 | 1622  |
| M31   | 1137  | 4    | 1141  |
| Total | 1442  | 1321 | 2763  |

The different orientations mean that symmetry about the midplane is imperfect, so the “bridge” region was taken as  $-20 < x < 30$  kpc. A count of stars in this region is shown in Table 3. This confirms that the largest populations are MW disk stars (mostly in a relatively dense tail) and M31 bulge stars (more widely dispersed).

**TODO** identify, trace history, trace fate

**TODO** Jacobi radius

**TODO** Tail kinematics:  $\sigma$ , energy

**TODO** Lifetime of tails

### 2.6.3. Mass transfer

Stars are scattered from galaxies even in normal times, and this can be expected to increase significantly during near-misses and collisions. To get a first impression of how many stars and DM particles may end up closer to a different galaxy, we looked at the relative distances of each particle to each of the three galaxy CoMs. It should be emphasized that kinematics is not considered at this stage, so nothing can be said about which particles are gravitationally bound.

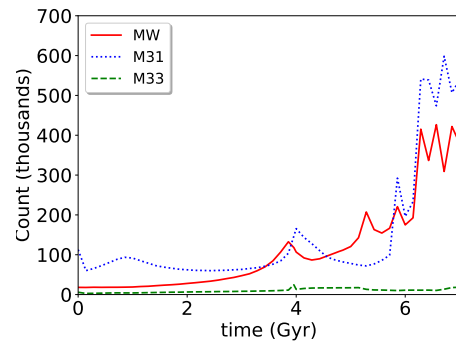


**Figure 20.** Particles closer to a different CoM.

Figure 20 shows that some particles are far from their notional galaxy even at the start. This increases somewhat during first pericenter around 4 Gyr, then jumps permanently during the second pericenter and merger. The plot cuts off at 7 Gyr because it becomes meaningless to consider the MW/M31 CoMs as separate points post-merger.

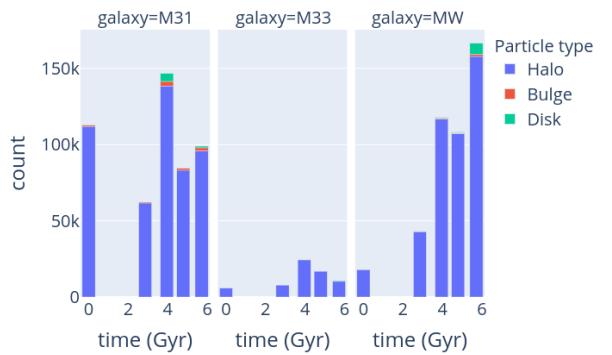


**Figure 21.** Particles closer to a different CoM.

Figure 21 looks at a few timepoints by particle type, showing that the overwhelming majority of these particles are from the DM halo. This is unremarkable, given

the prevalence of these particles at large radii and their correspondingly weak gravitational binding.

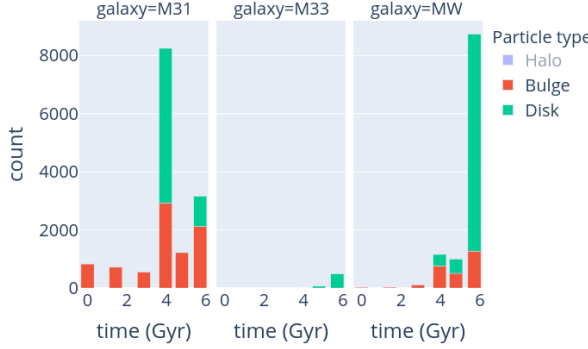


**Figure 22.** Luminous particles closer to a different CoM (DM halo hidden).

To focus on the baryonic matter, Figure 22 hides the DM halo and expands the  $y$ -axis to show only bulge and disk particles. There are significant numbers of M31 bulge particles at all timepoints, mostly reflecting the proximity of M33. The last three bars on each panel correspond to first pericenter, apocenter, and second pericenter. M31 disk particle numbers jump at first pericenter but these apparently remain bound to the original galaxy: virtually all return to M31 before apocenter.

### 2.7. MW-M31 merger

After second pericenter, the MW and M31 never fully separate and eventually merge. Their mass ratio is 1:1.6 for stellar matter and 1:1 when the DM halo is included. This is thus a ‘major merger’, which is generally taken to mean closer than 1:4 luminosity ratio (or mass ratio as a proxy). A 1:1 mass ratio has been reported (Boylan-Kolchin et al. 2008; Ji et al. 2014) to lead to the shortest coalescence time.

The 3D trajectories are complex, but Figures 23 and 24 are snapshots which attempts to show this. The MW CoM is always at the origin and the points show the M31 CoM at regular 14.3 Myr intervals. First pericenter is at upper left (outer), apocenter at the bottom, second pericenter in the tight reversal at upper left. The path is smooth up to 6.1 Gyr then becomes more chaotic.

TODO changes in mass profile

#### 2.7.1. Inclinations

TODO Relative rotation axes of disks – prograde?

### 2.8. Merger stellar remnant

#### 2.8.1. Remnant shape

TODO boxiness?

M31 relative to MW, colored by elapsed time (>3.8 Gyr)

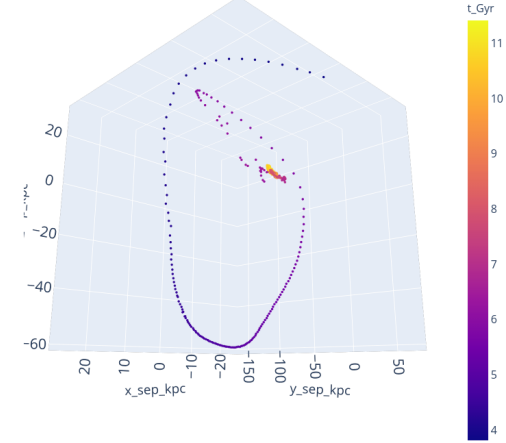


**Figure 23.** Approach and merger in a MW-centric coordinate frame. Points are spaced at 14.3 Myr intervals.).

M31 relative to MW, colored by separation distance

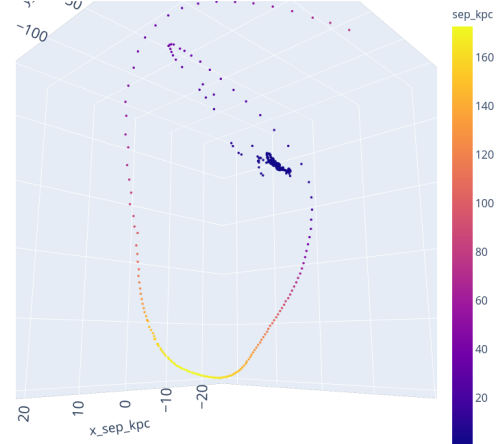


**Figure 24.** Approach and merger. Similar to Figure 23 except the color coding is by separation.

We can expect the remnant to settle over time into a triaxial ellipsoid TODO ref?. In observational astronomy it would be usual to determine the shape by fitting ellipses to surface brightness contours. That is also possible for the simulation, but for a highly-determined system for which we know the mass and position of every particle there are other options.

If we combine all the baryonic matter (disk and bulge) from both MW and M31, there are  $1.12 \times 10^6$  particles to consider. Some of these have been ejected to large radius where they have an exaggerated effect on the moment of inertia, so only those within 40 kpc of the CoM were

used in the calculation. These were about 88% of the original halo particles from the two precursor galaxies.

In the original coordinates, the moment of inertia tensor is symmetrical ( $I_{ij} = I_{ji}$ ),  $3 \times 3$ :

$$I = \begin{bmatrix} I_{xx} & I_{xy} & I_{xz} \\ I_{yx} & I_{yy} & I_{yz} \\ I_{zx} & I_{zy} & I_{zz} \end{bmatrix}$$

$$I_{\text{stellar}} \approx 10^3 \times \begin{bmatrix} 3.26 & 0.181 & 0.152 \\ 0.181 & 2.97 & 0.138 \\ 0.153 & 0.138 & 2.80 \end{bmatrix}$$

The orientation is arbitrary at this stage. To get principal axes we need the eigenvalues and eigenvectors of  $I$ .

The eigenvalues give the moments of inertia about the principal axes, in arbitrary units scaled such that  $A = 1$  and  $A \geq B \geq C$ :

$$A = 1.0, \quad B = 0.85, \quad C = 0.80$$

The eigenvectors give an orthonormal coordinate system oriented along the principal axes:

$$\hat{v}_a = \langle -0.844, -0.438, -0.309 \rangle$$

$$\hat{v}_b = \langle -0.524, +0.797, +0.302 \rangle$$

$$\hat{v}_c = \langle -0.114, -0.416, +0.902 \rangle$$

Determining the shape of a three-dimensional distribution of particles is known to have many subtleties (Macciò et al. 2007; Jing & Suto 2002). As a simple first approximation, the moment of inertia of an ellipsoid with semi-major axes  $a, b, c$  is  $A = k(b^2 + c^2)$  where  $k$  is a constant that depends on total mass. Other axes have the same form by symmetry. Solving for  $a, b, c$  and normalizing gives:

$$a = 1.0, \quad b = 0.94, \quad c = 0.77$$

So by this method the remnant is triaxial (low-symmetry, with  $a \neq b \neq c$ ). However, the minor axis  $c$  is significantly smaller than the other two: the ellipsoid is approximately prolate ( $a \approx b > c$ ).

Coordinates were rotated to place the eigenvector corresponding to the major axis along the  $z$ -axis. By chance, this left the other eigenvectors within  $7^\circ$  of the  $x$ - and  $y$ -axes. Orthogonal-view density plots are shown in Figure 25. In the mid and right panels the long axis of the density contours should be vertical, but this is clearly not the case. As Jing & Suto (2002) point out, the moment inertia tensor is sensitive to the outer boundary of the distribution. The 40 kpc spherical boundary used here is clearly too simplistic. It even

appears from Figure 25 that ellipticity varies with radius and is highest near the center; also that orientation varies with radius, with the outer contours having the long axis more vertical.

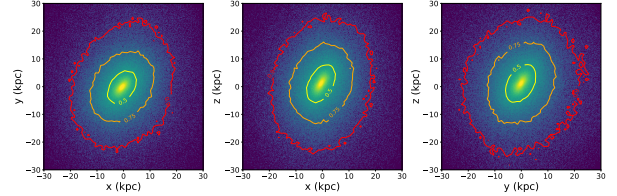


**Figure 25.** Density plot, oriented with the presumed major axis along  $z$ .

This topic will be revisited after the discussion of angular momentum in a later section.

### 2.8.2. Baryonic mass distribution

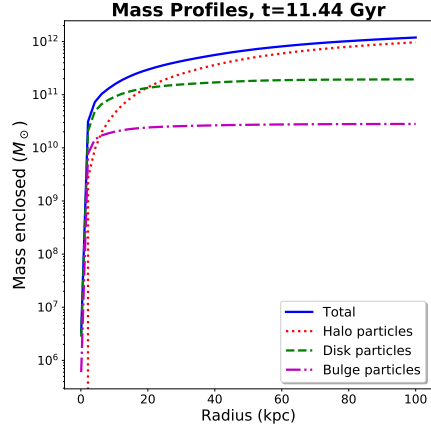


**Figure 26.** Mass profiles of the remnant by particle type.

The mass profile for each type of particle and overall is shown in Figure 26. This is similar to Figure 6, except that the radius now extends out to 100 kpc.

Previous sections have shown that MW and M31 particles remain somewhat distinct after merger. Figure 27 compares their mass profiles. For baryonic particles, ex-M31 masses are higher than ex-MW at most radii, reflecting the higher baryonic mass fraction in M31. The opposite effect might be expected for the DM halo, whose total mass was significantly higher in the MW (Table 2), but this is not seen out to 100 kpc. Figure 28 suggests we have to go almost 1 Mpc out before MW particles become the largest halo component.

**TODO Does stellar density profile agree with predictions for elliptical galaxies?**

Figure 31 shows Sérsic fits to the surface brightness profile (assuming  $M_*/L \sim 1$ ).

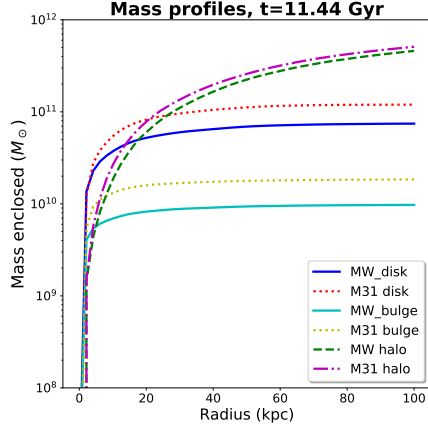


**Figure 27.** Mass profiles of the remnant by origin.

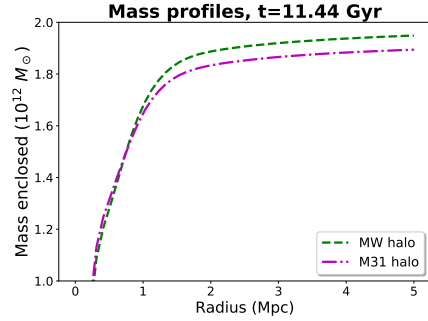


**Figure 28.** Mass profiles of the outer part of the remnant halo.

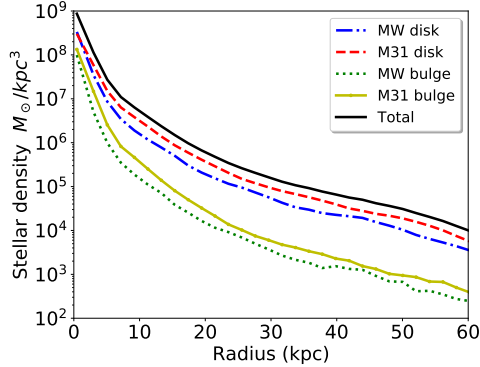


**Figure 29.** Spherically-averaged density profiles of the remnant luminous matter by origin.

The mass profile of DM particles in the remnant halo is well fit by a Hernquist profile, but there are some differences depending on origin as shown in Table 3

For comparison, the  $a$  values at  $t = 0$  were

$$\text{MW} = 61.6 \pm 0.5 \text{ kpc}$$

$$\text{M31} = 61.4 \pm 0.2 \text{ kpc}$$

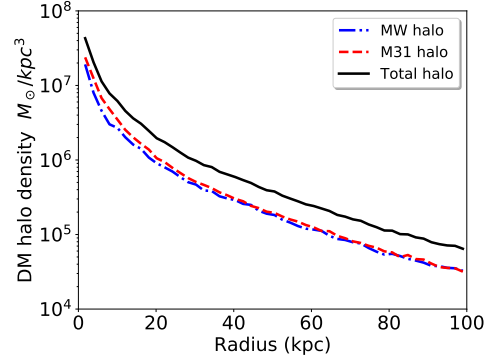


**Figure 30.** Spherically-averaged density profiles of the remnant halo by origin. Note the expanded  $x$ -axis relative to Figure 29

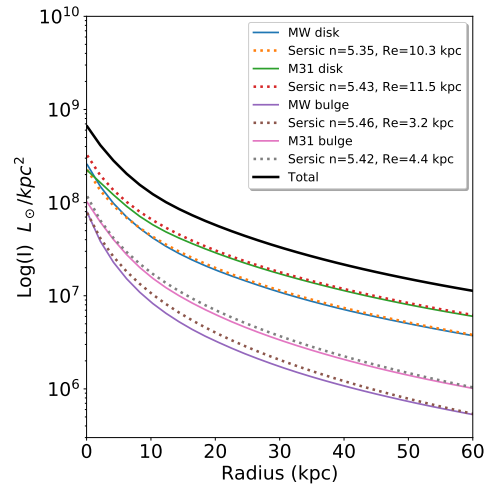


**Figure 31.** Surface brightness profiles of the remnant by origin.

**Table 3.** Best-fit Hernquist  $a$  for remnant halo

| Origin | $a \pm \text{StdDev}$ (kpc) |
|--------|-----------------------------|
| total  | $84.5 \pm 0.5$              |
| ex-MW  | $95.2 \pm 1.4$              |
| ex-M31 | $82.3 \pm 0.9$              |

The overall time-dependence of Hernquist radii was shown in Figure 16.

### 2.8.3. Angular momentum

The specific angular momentum  $\vec{h}$  was calculated for all the particles in the merger remnant and various subsets, as shown in Table 4. Differences tend to be small

for stellar particles regardless of origin, larger for the ex-M31 halo and much larger for the ex-MW halo.

We showed in Figure 17 that halo angular momentum mostly arises from tidal forces during close approach and merger, and in Figure 16 that MW halo particles subsequently have a significantly larger scale radius than M31 halo particles. As specific angular momentum is a product of radius and tangential velocity, it seems reasonable that we see a higher value for ex-MW Dark Matter when it tends to be at larger radius.

**Table 4.** Specific angular momentum components for the merger remnant at  $t=11.44$  Gyr ( $\text{kpc}^2 / \text{Myr}$ )

|           | $\hat{h}_x$ | $\hat{h}_y$ | $\hat{h}_z$ | $ h $ |
|-----------|-------------|-------------|-------------|-------|
| total     | 0.64        | 0.03        | -0.77       | 12.77 |
| MW disk   | 0.65        | -0.13       | -0.75       | 6.43  |
| M31 disk  | 0.53        | -0.21       | -0.82       | 6.28  |
| MW bulge  | 0.62        | -0.05       | -0.78       | 6.80  |
| M31 bulge | 0.61        | -0.12       | -0.78       | 6.22  |
| MW halo   | 0.66        | 0.09        | -0.74       | 16.89 |
| M31 halo  | 0.60        | -0.08       | -0.80       | 9.42  |

A previous section suggested that the remnant is elliptical but it is complex to define a precise shape from the mass distribution. An analysis of the angular momentum vector may provide an alternative approach.

Looking at subgroups of particle by origin, the mutual inclination angles are non-zero but generally quite small, as shown in Table 5.

**Table 5.** Mutual inclination angles for rotation vectors in the merger remnant at  $t=11.44$  Gyr (degrees)

|       | total | MWd  | M31d | MWb  | M31b | MWh  | M31h |
|-------|-------|------|------|------|------|------|------|
| total | —     | 9.0  | 15.5 | 4.5  | 8.9  | 4.2  | 6.9  |
| MWd   | 9.0   | —    | 9.2  | 5.4  | 3.2  | 12.7 | 4.9  |
| M31d  | 15.5  | 9.2  | —    | 11.0 | 7.0  | 19.7 | 8.7  |
| MWb   | 4.5   | 5.4  | 11.0 | —    | 4.5  | 8.7  | 2.4  |
| M31d  | 8.9   | 3.2  | 7.0  | 4.5  | —    | 13.1 | 2.7  |
| MWh   | 4.2   | 12.7 | 19.7 | 8.7  | 13.1 | —    | 11.1 |
| M31h  | 6.9   | 4.9  | 8.7  | 2.4  | 2.7  | 11.1 | —    |

That analysis used all particles origination from the MW and M31, regardless of distance from the CoM. To check the validity of this, we calculated how specific

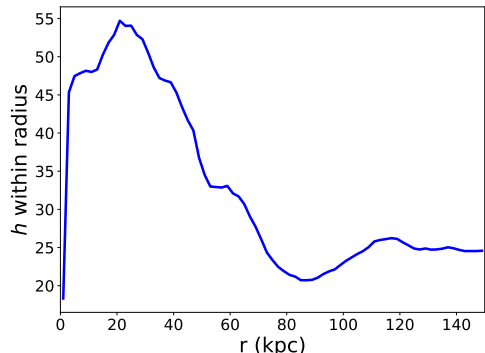


**Figure 32.** Stellar specific angular momentum of the MW-M31 remnant within various radii ( $h$  has arbitrary units).

angular momentum varies with radius. Attempting to do this for thin spherical shells gave surprisingly noisy results with no clear interpretation. Instead, Figure 32 shows values for all stars within various radii of the CoM. The profile is unexpectedly complex, with an apparent separation between inner and outer regions.

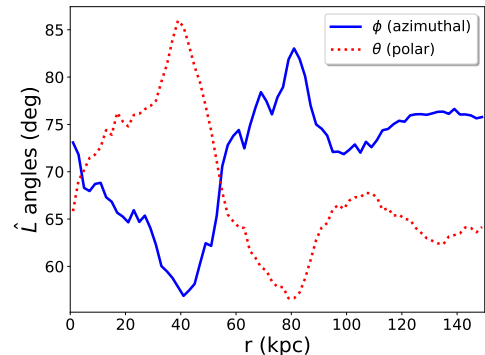


**Figure 33.** Stellar angular momentum orientation of the MW-M31 remnant within various radii (spherical coordinates).

To investigate this further, Figure 33 shows the orientation of  $\hat{L}(r)$  in spherical coordinates, where  $\phi$  is the azimuthal angle in the  $x, y$  plane and  $\theta$  is the polar angle downwards from the positive  $z$ -axis, as in Figure 34.<sup>5</sup> Again, we see a substantial variation by radius: the remnant is not rotating as a solid body. With the major caveat that we are looking at spherically-averaged values for a structure which probably has substantial (but at this point undefined) ellipticity, the remnant is clearly far from equilibrium and has a complex structure and kinematics.

<sup>5</sup> [https://en.wikipedia.org/wiki/Spherical\\_coordinate\\_system#/media/File:3D\\_Spherical.svg](https://en.wikipedia.org/wiki/Spherical_coordinate_system#/media/File:3D_Spherical.svg)

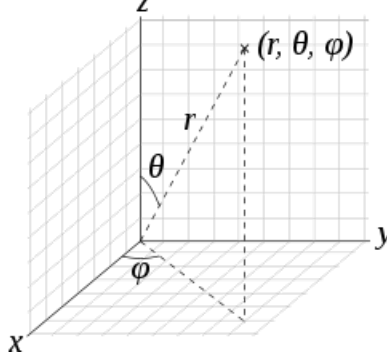


**Figure 34.** Spherical coordinate convention.

This collision and a single merger is not sufficient to randomize stars within the remnant. This is consistent with the understanding that relaxation times are very long in collisionless systems on the scale of elliptical galaxies (Binney & Tremaine 2008, Section 1.2). During the conditions of a galactic collision and merger there is an additional mechanism, called violent relaxation, that is significantly faster (Binney & Tremaine 2008, Section 4.10.2). Despite this, Barnes & Hernquist (1992) note that structure from the progenitors can survive the merging process. Also, there is observational evidence from rotation curves of elliptical galaxies that the inner and outer regions are sometimes decoupled, e.g. (Napolitano et al. 2002).

**TODO** distinguish by origin

#### 2.8.4. Remnant stellar kinematics

It was shown in (Cox et al. 2006) that simulated mergers lead to substantially different rotational kinematics if the galaxies are gas-poor (“dry”) and the collision is dissipationless versus gas-rich, dissipational collisions.

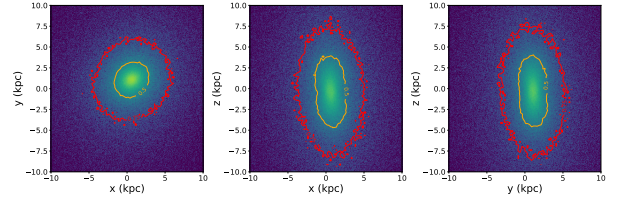
Initially, the stellar particles (from all origins) were used to calculate an angular momentum vector  $\hat{L}$ , then the coordinate system was rotated to place this along the  $z$ -axis. We might have expected the principal axes of the ellipsoid to correspond in some simple way to this projection, but this was found to be far from the case.

More intuitive results were obtained once the  $\hat{L}$  calculation was limited to stars within a limited radius of the CoM. Figure 35 uses a 50 kpc limit and shows that the major axis is approximately parallel to the rotation axis. Centering is clearly not perfect **TODO** can this be improved?

**TODO** Is it a fast or slow rotator?

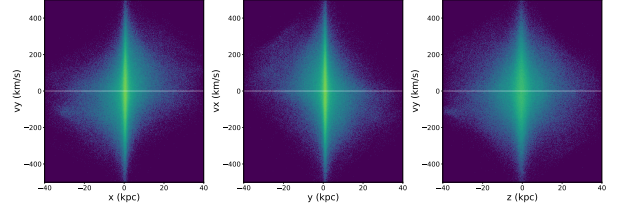
**TODO** Does the virial theorem work to return the total baryonic mass?

Figure 36 shows phase diagrams in various orientations. There is a fairly clear velocity asymmetry along



**Figure 35.** Luminous star density of the MW-M31 remnant in three orthogonal projections. Left panel looks down the  $\hat{L}$  axis, mid/right panels have this vertical.

the  $x$ - and  $y$ -axes, perpendicular to  $\hat{L}$ , but not along the  $z$ -axis.



**Figure 36.** Phase diagrams of the MW-M31 remnant, orthogonal views.

Mean radial velocities  $\bar{v}$  and velocity dispersions  $\sigma$  were calculated by binning along the  $y$ -axis (Figure 37) and the  $z$ -axis (Figure 38). The results are not entirely simple and regular, but the variation perpendicular to  $\hat{L}$  shows clear rotation with  $v_{\max} \approx 83$  km/s. As expected, along  $\hat{L}$  we see smaller and more random velocities with a somewhat higher dispersion.

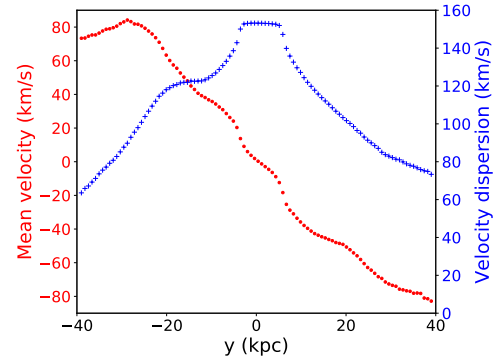


**Figure 37.** Velocity (red circles) and dispersion (blue +) by radius,  $y$ -axis: perpendicular to the angular momentum vector.

Central velocity dispersion is about 153 km/s, so the ratio  $v_{\max}/\sigma$  is 0.54.

For oblate isotropic rotators with ellipticity  $\epsilon$ , there is a relation **TODO** Binney78 ref

$$(V/\sigma) = \sqrt{\epsilon/(1-\epsilon)}$$

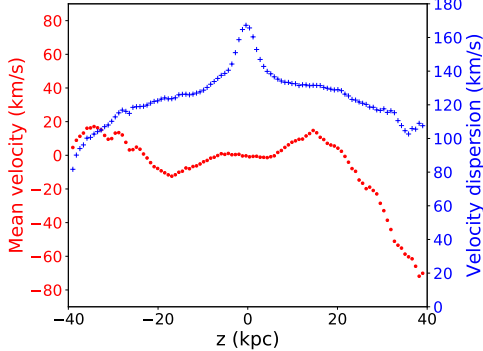


**Figure 38.** Velocity and dispersion by radius,  $z$ -axis: along the angular momentum vector.

For the stellar remnant we have  $\epsilon \approx 0.5$ , so  $(V/\sigma) \approx 1$ .

**TODO** Finish discussion

## 2.9. Merger DM halo remnant

### 2.9.1. Angular momentum

For the aggregate of all DM particles in the remnant at this time, the angular momentum vector has orientation  $\hat{h} = \langle 0.64, 0.03, -0.76 \rangle$ , almost identical to the total for all particles (baryonic + DM) in the remnant. The magnitude  $|h| = 13.15 \text{ kpc}^2/\text{Myr}$  is more than two orders of magnitude higher than the values for the individual galaxies about their respective CoM at the current epoch.

We showed in Figure 17 that halo angular momentum mostly arises from tidal forces during close approach and merger, and in Figure 16 that MW halo particles subsequently have a significantly larger scale radius than M31 halo particles. As specific angular momentum is a product of radius and tangential velocity, it seems reasonable that we see a higher value for ex-MW Dark Matter when it tends to be at larger radius.

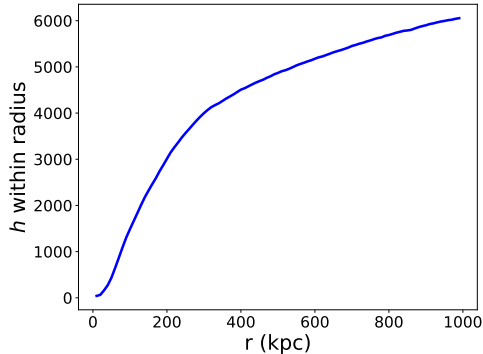


**Figure 39.** Halo specific angular momentum of the MW-M31 remnant within various radii ( $h$  has arbitrary units).

The radial dependency of angular momentum for stellar matter was previously shown to be complex (Figures 32 and 33). The analysis was repeated for the DM halo. Figures 39 and 40 show that any complexity is confined within about 60 kpc, where there is dense stellar matter. Outside this the profile is smooth to at least 1 Mpc.

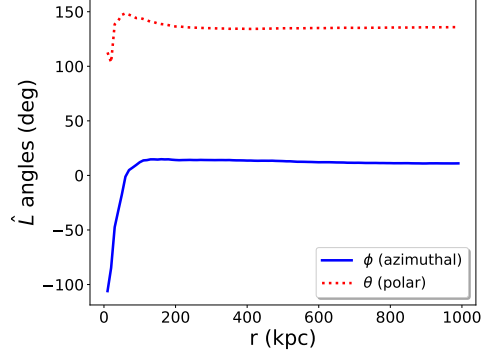


**Figure 40.** Halo angular momentum orientation of the MW-M31 remnant within various radii (spherical coordinates).

### 2.9.2. Virial radius

The DM halo obviously has no sharp outer edge, it just gradually fades into the inter-galactic medium (IGM). One popular convention is to use the  $r_{200}$  or “virial radius” as a limit: the radius at which the density is  $200 \times$  the cosmological critical density  $\rho_c$ .

For a flat LambdaCDM cosmology, we can calculate the critical density from

$$\rho_c(t) = \frac{3H^2(t)}{8\pi G}$$

Currently (PlanckCollaboration et al. 2016) we have<sup>6</sup>  $H(0) \equiv H_0 = 67.74 \text{ km/s/Mpc}$   $\rho_{c,0} = 127.35 M_\odot/\text{kpc}^3$

The simulation ends more than 11 Gyr in the future, so we need a different value for  $H(t)$ . By then the universe will be well into a Dark Energy-dominated epoch with near-exponential expansion. Then  $\dot{H}(t) \approx 0$  and  $H(t)$  asymptotically approaches its final value of  $H_\infty \approx 57 \text{ km/s/Mpc}$ .

This gives us a value of  $\rho_{c,\infty} \approx 90 M_\odot/\text{kpc}^3$ . Then  $r_{200}$  is the radius at which the spherically-averaged remnant halo density falls below  $1.8 \times 10^4 M_\odot/\text{kpc}^3$ . At the final timepoint, this is

$$r_{200} \approx 168 \text{ kpc}$$

<sup>6</sup> Wendy Freedman might disagree (very eloquently), but let’s go with these values for now.

The total virial mass, enclosed within the virial radius, is  $1.7 \times 10^{12} M_\odot$ , of which 87% is Dark Matter.

For comparison, if we used the current value  $\rho_{c,0}$  throughout, the virial radius at the final timepoint would be about 142 kpc and the virial mass falls to about  $1.5 \times 10^{12} M_\odot$ .

**TODO** Some discussion would be useful!

### 2.9.3. Remnant halo kinematics

The literature consensus is that halo shapes are supported by anisotropic velocity dispersions, not spin (Frenk & White 2012). They can acquire angular momentum through tidal torques, as we already saw for each galaxy in Figure 17. This is often characterized by a dimensionless spin parameter:

$$\lambda = \frac{J|E|^{1/2}}{GM^{5/2}}$$

where  $J$  is the magnitude of the angular momentum vector,  $E$  is the total energy and  $M$  is the halo mass. Often, these are taken as the values inside the virial radius, ignoring DM particles lost to the IGM.

Total energy  $E$  is the sum of kinetic energy  $K$  and potential energy  $W$ . We have the mass and velocity of every particle so

$$K = \sum_i \frac{1}{2} m_i v_i^2$$

Potential energy is more challenging to calculate. In general (Binney & Tremaine 2008, section 2.1):

$$W = \frac{1}{2} \int d^3 \mathbf{x} \rho(\mathbf{x}) \Phi(\mathbf{x})$$

We would need this to calculate the highly-disrupted situation shortly after collision and merger (Binney & Tremaine 2008, section 8.2). For simplicity, we concentrate here on the final timepoint about 5 Gyr after merger, and assume that the remnant halo is by then close to virial equilibrium. Then  $E \approx -K$  and the calculation is very much easier.

Other than potential energy, relevant values for the remnant halo vary little over time. Figure 41 shows that angular momentum, kinetic energy and virial mass remain within  $\pm 20\%$  of their final value.

The final timepoint of the simulation gives these results:

$$J = 2.9 \times 10^{12} M_\odot \text{kpc}^2/\text{Myr}$$

$$K = 1.5 \times 10^{65} \text{ erg}$$

$$M = 1.3 \times 10^{12} M_\odot$$

Unfortunately, this gives a spin parameter  $\lambda \approx 30$ , about 2 orders of magnitude higher than expected.

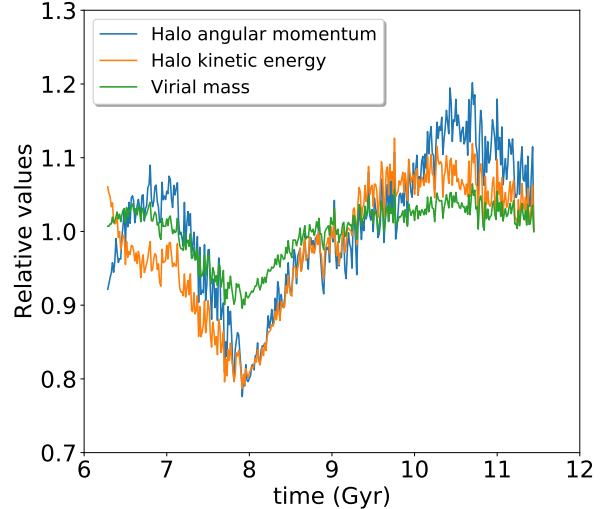


**Figure 41.** Relative values for the remnant halo over time; final timepoint = 1.

**TODO** Figure out what went wrong!

**TODO** remnant DM  $\sigma$

**TODO**  $V_{\text{esc}}(r)$

## 3. DISCUSSION AND CONCLUSIONS

**TODO** add some!

## 4. ACKNOWLEDGMENTS

The author is grateful to Professor Gurtina Besla for teaching the class on which this paper is based and for allowing this rather geriatric student to participate, as well as providing all the raw data from the earlier simulation described in vdM12. Also to Rixin Li for valuable coding advice. Finally, the Astronomy majors deserve my thanks for patient and supportive interactions with a fellow student older than their parents, during the past four semesters. I wish them every success in the future!

This work relied on a range of open-source software packages, many of them sponsored by NumFOCUS<sup>7</sup> for the benefit of us all:

- NumPy (van der Walt et al. 2011)
- Matplotlib (Hunter 2007)
- pandas (McKinney 2010)
- Astropy (Astropy Collaboration et al. 2013)
- SciPy (Virtanen et al. 2020)
- IPython (Perez & Granger 2007)
- Jupyter (Kluyver et al. 2016)
- conda-forge<sup>8</sup>

<sup>7</sup> <https://numfocus.org/>

<sup>8</sup> <https://conda-forge.org/>

Additionally, mpl-scatter-density<sup>9</sup> and Plotly<sup>10</sup> were used in preparing the figures.

## REFERENCES

- Astropy Collaboration, Robitaille, T. P., Tollerud, E. J., et al. 2013, A&A, 558, A33, doi: [10.1051/0004-6361/201322068](https://doi.org/10.1051/0004-6361/201322068)
- Barnes, J. E., & Hernquist, L. 1992, Annual Review of Astronomy and Astrophysics, 30, 705, doi: [10.1146/annurev.aa.30.090192.003421](https://doi.org/10.1146/annurev.aa.30.090192.003421)
- Binney, J., & Tremaine, S. 2008, Galactic Dynamics: Second Edition, by James Binney and Scott Tremaine. ISBN 978-0-691-13026-2 (HB). Published by Princeton University Press, Princeton, NJ USA, 2008. <http://adsabs.harvard.edu/abs/2008gady.book.....B>
- Bodenheimer, P., Laughlin, G. P., Różyczka, M., & Yorke, H. W. 2007, Numerical Methods in Astrophysics: An Introduction (CRC Press). <http://adsabs.harvard.edu/abs/2007nmai.conf.....B>
- Boylan-Kolchin, M., Ma, C.-P., & Quataert, E. 2008, Monthly Notices of the Royal Astronomical Society, 383, 93, doi: [10.1111/j.1365-2966.2007.12530.x](https://doi.org/10.1111/j.1365-2966.2007.12530.x)
- Brown, A. G. A., Vallenari, A., Prusti, T., et al. 2018, Astronomy & Astrophysics, 616, A1, doi: [10.1051/0004-6361/201833051](https://doi.org/10.1051/0004-6361/201833051)
- Cox, T. J., Dutta, S. N., Di Matteo, T., et al. 2006, The Astrophysical Journal, 650, 791, doi: [10.1086/507474](https://doi.org/10.1086/507474)
- de Vaucouleurs, G. 1948, Annales d'Astrophysique, 11, 247. <http://adsabs.harvard.edu/abs/1948AnAp...11..247D>
- Frenk, C. S., & White, S. D. M. 2012, Annalen der Physik, 524, 507, doi: [10.1002/andp.201200212](https://doi.org/10.1002/andp.201200212)
- Hernquist, L. 1990, The Astrophysical Journal, 356, 359, doi: [10.1086/168845](https://doi.org/10.1086/168845)
- Hunter, J. D. 2007, Computing in Science & Engineering, 9, 90, doi: [10.1109/MCSE.2007.55](https://doi.org/10.1109/MCSE.2007.55)
- Ji, I., Peirani, S., & Yi, S. K. 2014, Astronomy & Astrophysics, 566, A97, doi: [10.1051/0004-6361/201423530](https://doi.org/10.1051/0004-6361/201423530)
- Jing, Y. P., & Suto, Y. 2002, The Astrophysical Journal, 574, 538, doi: [10.1086/341065](https://doi.org/10.1086/341065)
- Kluyver, T., Ragan-Kelley, B., Pérez, F., et al. 2016, in Positioning and Power in Academic Publishing: Players, Agents and Agendas, ed. F. Loizides & B. Schmidt, IOS Press, 87 – 90
- Macciò, A. V., Dutton, A. A., van den Bosch, F. C., et al. 2007, Monthly Notices of the Royal Astronomical Society, 378, 55, doi: [10.1111/j.1365-2966.2007.11720.x](https://doi.org/10.1111/j.1365-2966.2007.11720.x)
- Marel, R. P. v. d., Besla, G., Cox, T. J., Sohn, S. T., & Anderson, J. 2012a, The Astrophysical Journal, 753, 9, doi: [10.1088/0004-637X/753/1/9](https://doi.org/10.1088/0004-637X/753/1/9)
- Marel, R. P. v. d., Fardal, M., Besla, G., et al. 2012b, The Astrophysical Journal, 753, 8, doi: [10.1088/0004-637X/753/1/8](https://doi.org/10.1088/0004-637X/753/1/8)
- Marel, R. P. v. d., Fardal, M. A., Sohn, S. T., et al. 2019, The Astrophysical Journal, 872, 24, doi: [10.3847/1538-4357/ab001b](https://doi.org/10.3847/1538-4357/ab001b)
- McKinney, W. 2010, in Proceedings of the 9th Python in Science Conference, ed. Stéfan van der Walt & Jarrod Millman, 56 – 61, doi: [10.25080/Majora-92bf1922-00a](https://doi.org/10.25080/Majora-92bf1922-00a)
- Mo, H., van den Bosch, F. C., & White, S. 2010, Galaxy Formation and Evolution, by Houjun Mo , Frank van den Bosch , Simon White, Cambridge, UK: Cambridge University Press, 2010. <http://adsabs.harvard.edu/abs/2010gfe..book....M>
- Napolitano, N. R., Arnaboldi, M., & Capaccioli, M. 2002, Astronomy & Astrophysics, 383, 791, doi: [10.1051/0004-6361:20011795](https://doi.org/10.1051/0004-6361:20011795)
- Perez, F., & Granger, B. E. 2007, Computing in Science & Engineering, 9, 21, doi: [10.1109/MCSE.2007.53](https://doi.org/10.1109/MCSE.2007.53)
- PlanckCollaboration, Ade, P. A. R., Aghanim, N., et al. 2016, Astronomy & Astrophysics, 594, A13, doi: [10.1051/0004-6361/201525830](https://doi.org/10.1051/0004-6361/201525830)
- Rubin, V. C., & Ford, Jr., W. K. 1970, The Astrophysical Journal, 159, 379, doi: [10.1086/150317](https://doi.org/10.1086/150317)
- Sérsic, J. L. 1963, Boletín de la Asociacion Argentina de Astronomía La Plata Argentina, 6, 41. <http://adsabs.harvard.edu/abs/1963BAAA....6...41S>
- Toomre, A., & Toomre, J. 1972, The Astrophysical Journal, 178, 623, doi: [10.1086/151823](https://doi.org/10.1086/151823)
- van der Walt, S., Colbert, S. C., & Varoquaux, G. 2011, Computing in Science & Engineering, 13, 22, doi: [10.1109/MCSE.2011.37](https://doi.org/10.1109/MCSE.2011.37)
- Virtanen, P., Gommers, R., Oliphant, T. E., et al. 2020, Nature Methods, doi: <https://doi.org/10.1038/s41592-019-0686-2>
- Zwicky, F. 1933, Helvetica Physica Acta, 6, 110. <http://adsabs.harvard.edu/abs/1933AcHPh...6..110Z>
- . 1955, Publications of the Astronomical Society of the Pacific, 67, 232, doi: [10.1086/126807](https://doi.org/10.1086/126807)

<sup>9</sup> <https://github.com/astrofrog/mpl-scatter-density>

<sup>10</sup> <https://plotly.com/python/>